Carbon Letters (2022) 32:999–1015
https://doi.org/10.1007/s42823-022-00333-x

Online ISSN 2233-4998
Print ISSN 1976-4251

ORIGINAL ARTICLE

Photoelectrochemical and electrochemical urea oxidation with microwave-assisted synthesized Co-Fe_2O_3@NiO core–shell nanocomposites

Assia Karrab[1] · **Remi Bensimon**[2] · **Diane Muller**[2] · **Stéphane Bastide**[2] · **Christine Cachet-Vivier**[2] · **Salah Ammar**[1]

Received: 26 January 2022 / Revised: 22 February 2022 / Accepted: 1 March 2022 / Published online: 15 March 2022

Abstract

This work reported the electrochemical and photoelectrochemical (PEC) properties of a new photoelectrode based on hematite Co-Fe_2O_3@NiO, a photoactive semiconductor, was prepared using a process involving a combination of the co-precipitation and microwave-assisted synthesis of Fe_2O_3, Co-Fe_2O_3 and Co-Fe_2O_3@NiO, respectively. The obtained products were characterized by X-Ray powder Diffraction (XRD), Scanning Electron Microscope (SEM), Energy Dispersive X-ray analysis (EDX), Ultraviolet–Visible (UV–vis) analysis, Fourier Transform Infrared spectroscopy (FT-IR). X-ray diffraction (XRD) pattern of the sample determined the crystal structure of α-Fe_2O_3 nanoparticles. The SEM image shows spherical nanoparticles. FTIR spectrospy spectrum confirmed the phase purity and chemical bond for the sample. Optical studies show a variation of band gap from 2.118 to 2.07 eV. The electrochemical and photoelectrochemical (PEC) performance of the films were examined by cyclic voltammetry, linear sweep voltammetry and chronoamperometry. The electrochemical oxidation of water achieved by Cobalt-doped Fe_2O_3@GCE modified electrode exhibited the current density of 21 mA/g at 0.5 V vs. SCE for 5 at% of Co and reveals enhanced specific capacitance of 352.11 F/g. The catalytic performance of urea oxidation was measured by cyclic voltammetry on Co-Fe_2O_3@NiO nanoparticles modified glassy carbon electrode (GCE) in alkaline medium. The electrode Co-Fe_2O_3@NiO without annealing showed a peak current density of 1.59 mA/cm^2 at 0.1 M urea in 1.0 M NaOH, which was 3.6 fold higher than that of Co-Fe_2O_3@NiO with annealing. In another part, this work reported the photoelectrochemical (PEC) properties of photoanode prepared by spin coating. The highest photocurrent 0.042 mA/cm^2 at 0.5 V Vs SCE was obtained for 5% Co-Fe_2O_3@NiO while the photocatalytic oxidation of urea.

Keywords Hematite · Urea · Nickel · Glassy carbon electrode (GCE) · Photoelectrochemical oxidation

1 Introduction

Global energy consumption is steadily rising as a result of population increase and the demand for social well-being for the maximum number of people. The annual rate of energy consumption was roughly 13.5 TW in 2001, and it is predicted to rise to 27 TW (terawatts) by 2050, as fossil fuel combustion meets 85% of our energy needs [1, 2]. According to reports, the United Arab Emirates, one of the world's largest oil exporters, will be unable to meet the demand for oil and natural gas by 2015 and 2042, respectively [3]. When we take a step back from the status of our planet's ecosystem, it becomes evident that the majority of the world's ecological problems are actually energy issues. Climate change, for example, and all of its ramifications for the world are inextricably related to the energy dilemma, because the energies we consume (fossil fuels) are what caused the greenhouse effect and CO_2 emissions. According to the 2017 IEA report, worldwide CO_2 emissions attributable to fuel combustion alone decreased from 15,458 million tons in 1973 to 32,249 million tons in 2015. In addition, during our lifetime, huge amounts of domestic and industrial wastewater, which usually contain organic matter, are produced. Traditional methods of treating this wastewater consume a lot of energy. Although wastewater

---

✉ Assia Karrab
karrab_assia@yahoo.fr

[1] Matériaux Et Environnement UREME (UR17ES45), Faculté Des Sciences de Gabès, Unité de Recherche Electrochimie, Université de Gabès, Cité Erriadh, 6072 Gabès, Tunisia

[2] CNRS, Univ Paris Est Creteil, ICMPE, UMR7182, Thiais, France

treatment is currently considered a large consumer of energy. To solve these problems, the green movement has generally turned to a solution: renewable energies [4, 5].

Hydrogen is a clean energy resource, converting solar energy into chemical energy in the form of "solar fuels"; H_2 is seen as one of the most forward-looking strategies for solving the energy and environmental problems in the world. In the future, the production, storage and transport of hydrogen still suffer from great challenges which severely restrict the large-scale application of hydrogen energy.

Light-driven photoelectrochemical (PEC) water splitting is a promising pathway for conversion of solar energy to chemical energy and renewable [6], clean hydrogen production. The combining of photovoltaic cells with an electrolysis system represents a prospective alternative to hydrogen production from photoelectrochemical water splitting [7, 8]. The key strategy for realizing high-efficiency PEC water splitting is developing efficient semiconductor materials to absorb more solar energy.

Since TiO_2 electrode has been demonstrated that could be water split into H_2 and O_2 for the first time by Fujishima and Honda in a photoelectrochemical (PEC) cell under light illumination. To solve the energy crisis, great efforts have been devoted to developing diverse semiconductor photoelectrodes due to its potential as one of the clean, low-cost, and environmentally friendly strategies. Various semiconductor materials, such as Fe_2O_3 [9] WO_3 [10–12], $BiVO_4$ [13, 14], TiO_2 [15, 16], ZnO [17, 18], Cu_2O [19] and $SrTiO_3$ [20] have been considered as photoanodes in PEC water splitting systems. Fe_2O_3 is a promising semiconductor metal oxide that has received a lot of attention due to its admirable characteristics such as non-toxic, excellent stability, economical, chemically synthesized stable and profitable, low cost, high corrosion resistance and its moderate difference (~2 eV) [21, 22] allowing capturing ~40% of sunlight. Unlike other water pollutants, urea can be harnessed as a rich source of hydrogen. Typically, hydrogen can be exploited as a rich source of hydrogen. Primarily, the main constituent of human or animal waste on earth is urine, containing about 2–2.5% by weight of urea [23]. As a potential source of hydrogen and fuel, urea has a high energy density (16.9 MJ L^{-1}), high solubility (1079 g L^{-1}, 20 °C) [24], and content of in relatively high hydrogen (10.1% by weight) [25].

In the current work, we were developed new photoelectrodes based on hematite Co-Fe_2O_3@NiO, a photoactive semiconductor, prepared using a process involving a combination of co-precipitation and microwave-assisted synthesis for the synthesis of Co-Fe_2O_3 and Co-Fe_2O_3@NiO, respectively. The purpose of the present work is to gain more insight into the characterization of the electrocatalytic oxidation of urea on Co-Fe_2O_3@NiO nanoparticles modified GC electrode in alkaline medium. In addition, the study of the deposition by spin coating of synthesized powders for the photoelectrochemical water and urea oxidation.

2 Experimental

2.1 Materials

Iron (III) chloride hexahydrate ($FeCl_3.6H_2O$, 97%), aqueous ammonia solution (99%) at 28%, Cobalt (II) chloride hexahydrate ($CoCl_2.6H_2O$, 97%), Nickel (II) chloride ($NiCl_2.6H_2O$, 98%), ethylene glycol and ethanol were purchased from Sigma-Aldrich. All of the solutions were prepared with ultrapure water.

2.2 Synthesis of pure, Co-doped α-Fe_2O_3 and Co-Fe_2O_3@NiO nanoparticles

Nanoparticles of pure iron oxide (α-Fe_2O_3) and α-Fe_2O_3 Co-doped (1%, 5% and 10% molar) were prepared by co-precipitation method. At the start, 0.15 M $FeCl_3.6H_2O$ was dissolved in 100 mL of ultrapure water for 30 min at a temperature of 80 °C. Different amounts of $CoCl_2.6H_2O$ were then added to the solution. Then an aqueous ammonia solution was added until a pH value of 11 and the solution was kept for 3 h to completely obtain the hydroxide phase. After cooling to room temperature, the precipitate obtained was centrifuged and washed with ethanol and ultrapure water. A drying step at 80 °C for 12 h was followed by an annealing step at 800 °C for 4 h. In the second step, 1 mmol of powdered Co-Fe_2O_3 is added to the solution of 1 mmol of nickel (II) chloride hexahydrate mixed in 7 mL of alcohol and 3 mL of EG, which is then dispersed by ultrasound for about 15 min. The mixture obtained is transferred to an autoclave, and then transferred to a microwave (Microwave digestion system: Multiwave GO Plus). After completing the interaction (irradiation time of 60 min at 200 °C), the precipitate is washed by water and ethanol, dried at 80 °C for 12 h to obtain $Fe_2O_3/Ni(OH)_2$ core/shell nanocomposites. Then, with a heating rate of 5 °C/min for 3 h in a tube furnace, the product is calcined in air at 300 °C.

2.3 Preparation of α-Fe_2O_3, Co-Fe_2O_3 and Co-Fe_2O_3@NiO nanoparticles modified GC electrode

Electrochemical tests were performed by cyclic voltammetry (CV), using a three-electrode cell system. The GC electrode, platinum wire, and a saturated calomel electrode (SCE) were used as the working electrode, a counter electrode, and a reference electrode, respectively. The GC electrode, the surface area of 0.071 cm^2, must be polished with an alumina suspension on a mirrored surface, and treated with deionized water before each use. Then, 20 mg of active materials was

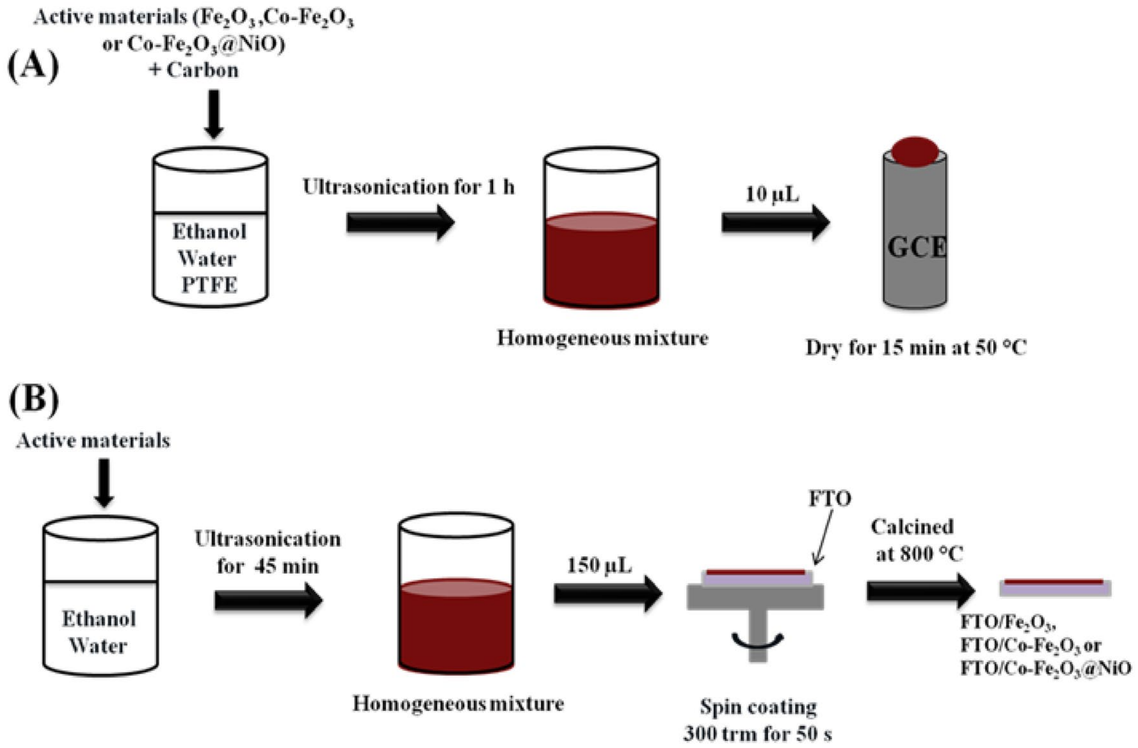

Scheme 1 Schematic representation for the synthesis **A** modified GCE and **B** the films by spin coating of Fe_2O_3, Co-Fe_2O_3 and Co-Fe_2O_3@NiO

measured to disperse in 40 mg of absolute ethanol with 2% carbon (High Surface Area Graphite 500 M^2g^{-1}) and 4% PTFE. The active materials were completely dispersed in 2.4 g of water under ultrasonication for 1 h. It was then 10 µL of active material on cleaned GCE, resulting 2.13 mg/cm^2 of active material loaded on the surface of GCE. The fabricated modified electrode was left to dry for 15 min at 50 °C (Scheme 1A). The dried electrode was used as the working electrode in electrochemical tests. The electrodes are connected to an AUTOLAB PGSTAT 100 potentiostat controlled by GPES software. CV tests, both with and without 0.1 mol/L urea, were performed at a scan rate of 10 mVs^{-1} in 1 M NaOH solution.

2.4 Preparation of the α-Fe_2O_3, Co-Fe_2O_3 and Co-Fe_2O_3/NiO films

To investigate the PEC performance of the synthesized bare, Co doped hematite and Co-Fe_2O_3/NiO nanostructures, initially fluorine-doped tin oxide (FTO) glass plate was ultrasonicated for 30 min in water and ethanol respectively. Then, a mixture consisting of 3.2 mg of sample, 0.5 mL of ethanol and 0.5 mL of deionized water was ultrasonicated for 45 min to obtain a suspension which was applied to the FTO plate by using 150 µL pipette in the active area 1 × 2 cm by spin coating (300 trm for 50 s) (Scheme 1B) and then dried to obtain the photoanode ready to take PEC measurement.

2.5 Characterization

The crystal structure, phase formation and purity of the synthesized powders were confirmed by powder XRD analysis using German Bruker D2 PHASER X-ray diffractometer with CuKa radiation (1.5418 Å) as a source. The intensity data were collected over the range of 15°–80°. The morphology was observed by SEM with a Merlin FEG microscope from Zeiss and the presence of Co and Ni in Co-Fe_2O_3 and Co-Fe_2O_3/NiO were confirmed by EDX analysis. Fourier Transform Infra-Red (FT-IR) spectra of samples were explored by a NICOLET IR200 FT-IR spectrometer. Diffuse reflectance spectra were recorded in solid state using UV–vis spectrophotometer U-4100 DEGETAL.

2.6 Electrochemical and photoelectrochemical measurements

To analyze the samples' OER activity, electrochemical measurements were done in a typical 3-electrode cell using an AUTOLAB PGSTAT 100 potentiostat controlled by GPES software. The counter and reference electrodes were platinum (Pt) wire and calomel electrode saturated with KCl (SCE), respectively. The working electrode was a glassy carbon electrode (GCE). The electrochemical performance (Scheme 2A) of OER activity was studied using cyclic voltammetry (CV), linear sweep voltammetry (LSV),

Scheme 2 Schematic representation of **A** electrochemical and **B** photoelectrochemical characterizations

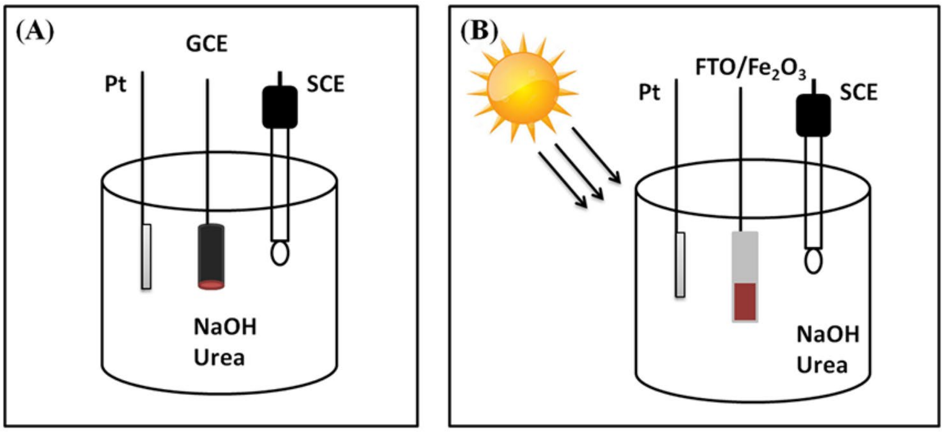

and chronoamperometry (CA). All tests were carried out with a 1 M NaOH electrolyte in the presence and absence of urea (0.1 M). As well as the shaping of nanoparticles in film form by the spin coating method for the photoelectrochemical water and urea oxidation (Scheme 2B), with a 500 W/m^2 OSRAM spot as a light source, the curves were obtained in both dark and under illumination.

3 Result and discussion

3.1 Structural analysis

The X-ray diffraction (XRD) is carried out to characterize and examine the structure, formed phases and crystallinity of the as-synthesized materials. Figure 1 shows the XRD patterns of pure and Co-doped hematite nanoparticles. For the α-Fe$_2$O$_3$ sample, the peaks located at 24.01°, 33.34°, 35.87°, 40.66°, 49.46°, 53.94°, 57.61°, 62.70°, 64.09°, 72.04° and 75.11°, can be indexed as the (112), (104), (110), (113), (024), (116), (018), (214), (300), (1010), and (220) planes, respectively, which can be perfectly matched with the diffraction peaks of hexagonal structured α-Fe$_2$O$_3$ [26] (JCPDS card no. 33-0664) [27]. The absence of β-FeOOH diffraction peaks indicates the complete conversion of iron oxyhydroxides to hematite. In addition, the peaks observed at 29.90°, 42.92° and 57.15° correspond to the crystallographic planes (220), (400) and (511), can be associated with cobalt oxide (JCPDS card no. 01–078-1969) [28].

The average crystallite size of pure and Co-doped α-Fe$_2$O$_3$ was calculated by Scherrer's formula:

$$D = \frac{0,9\lambda}{\beta\cos\theta}, \tag{1}$$

where λ, β, and θ stand for wavelength of X-ray, full-width at half maximum intensity, and Bragg's angle, respectively, using the most intense diffraction peak at (104). The estimated crystallite size of pure α-Fe$_2$O$_3$ and α-Fe$_2$O$_3$ (1, 5 and 10% Co) are 38 nm and (49, 50 and 52 nm) respectively (Table 1). The average particle size of these samples is clearly in the nanoscale domain, it increases with increasing doping concentration, which means that the addition of Co can effectively support the α-Fe$_2$O$_3$ crystalline grain growth.

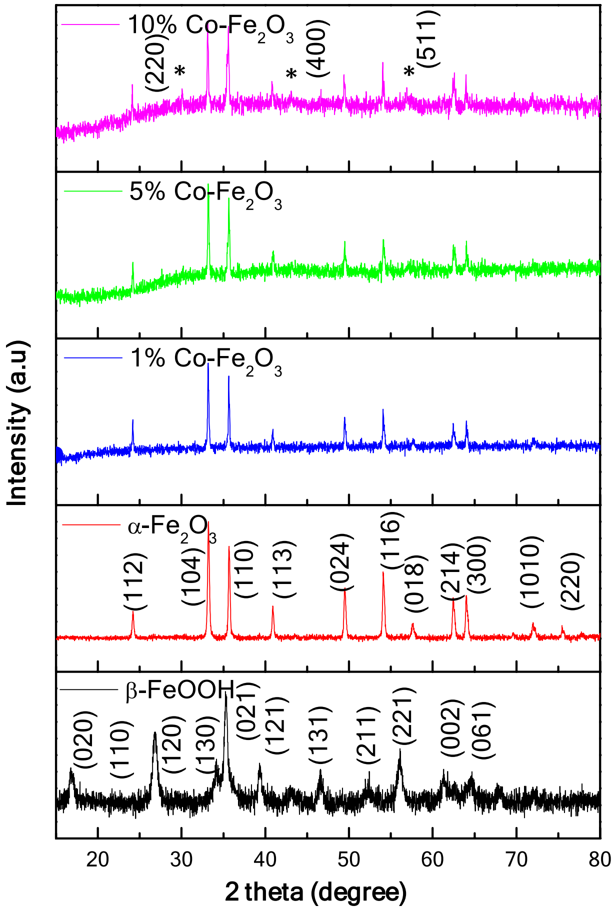

Fig. 1 X-ray diffraction spectra of β-FeOOH, undoped and Co-doped α-Fe$_2$O$_3$ nanoparticles with different Co doping contents

Table 1 Calculated crystallite size of the obtained products

Sample	Pos. [°2θ]	(h k l)	FWHM [°2θ]	Crystallite size (nm)
Undoped	33.21	(1 0 4)	0.229	38
1% Co-Fe_2O_3	33.18	(1 0 4)	0.168	49
5% Co-Fe_2O_3	33.20	(1 0 4)	0.165	50
10% Co-Fe_2O_3	33.13	(1 0 4)	0.156	52

The difference in size of the ionic radii of Co^{2+} (0.078 nm) and Fe^{3+} (0.067 nm) ions helps explain this phenomenon [29].

3.2 SEM observations/EDX

The morphology was further investigated using SEM. The corresponding, collected images are shown in Figs. 2 and 3. Figure 2 indicated the formation of spherical nanoparticles. It is clear that there is a variation in size with the percentage of dopant. The average particle size was calculated

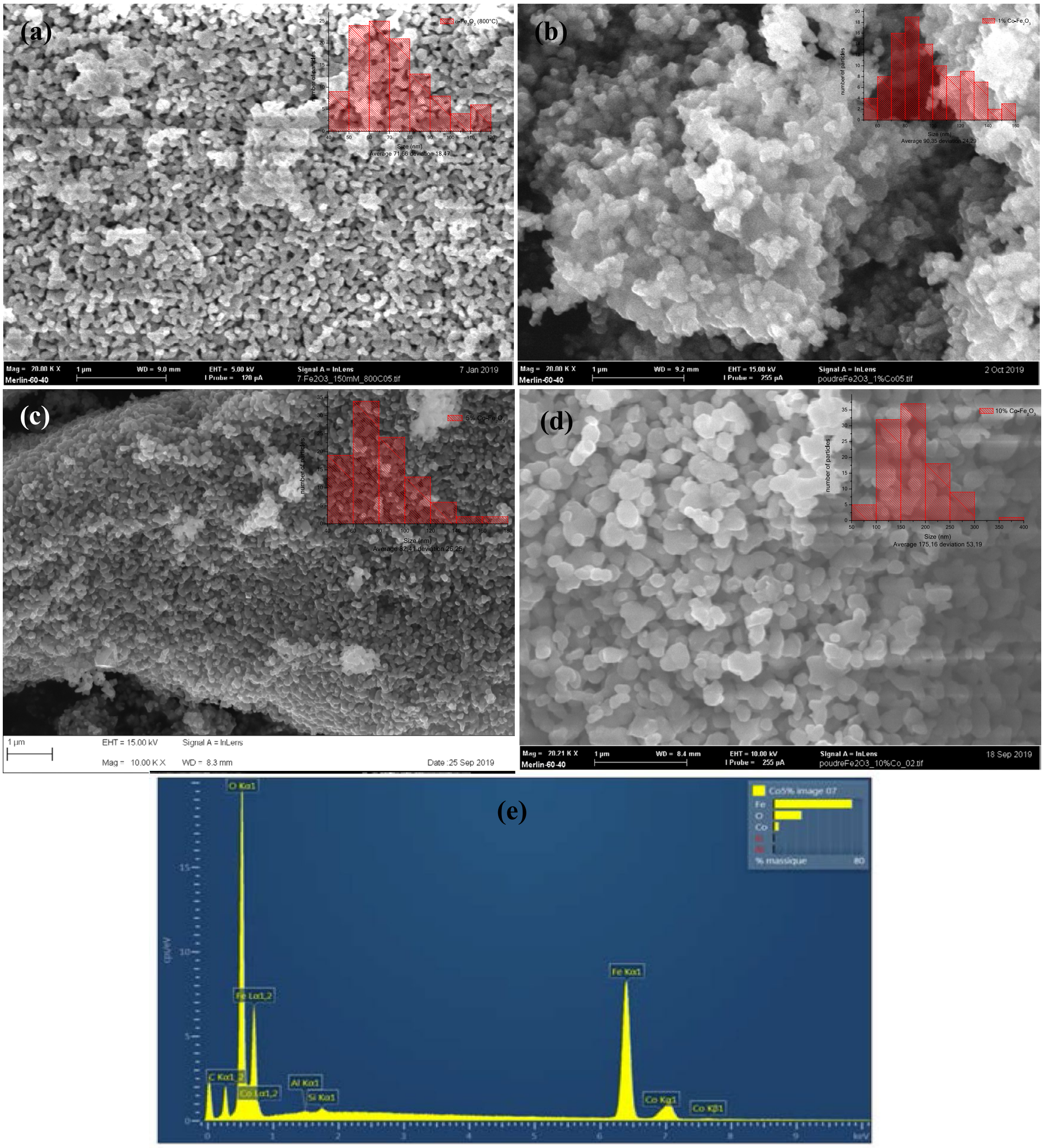

Fig. 2 MEB images with inset distribution profile of **a** Fe_2O_3, **b** 1% Co-Fe_2O_3, **c** 5% Co-Fe_2O_3 and **d** 10% Co-Fe_2O_3 and **e** the EDS spectrum for the Co doped α-Fe_2O_3

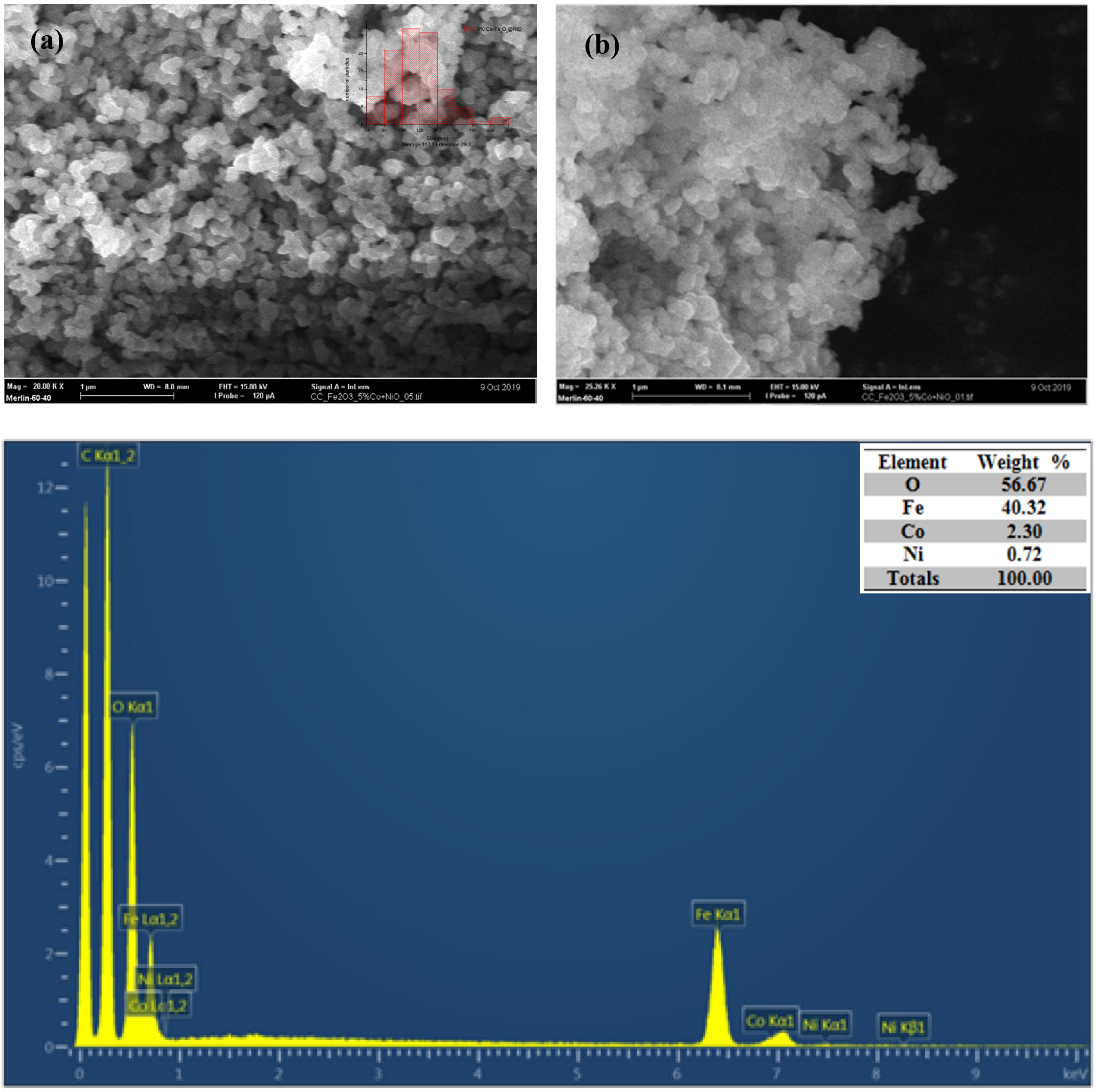

Element	Weight %
O	56.67
Fe	40.32
Co	2.30
Ni	0.72
Totals	100.00

Fig. 3 **a**, **b** MEB images with inset distribution profile and **c** EDX spectrum of 5% Co-Fe$_2$O$_3$@NiO

Table 2 Average size and deviation calculate with IMAGE-J software of α-Fe$_2$O$_3$, 1% Co-Fe$_2$O$_3$, 5% Co- Fe$_2$O$_3$, 10% Co-Fe$_2$O$_3$ and 5% Co-Fe$_2$O$_3$@NiO nanoparticles

Sample	Average size (nm)	Deviation (nm)
α-Fe$_2$O$_3$	71.66	18.47
1% Co-Fe$_2$O$_3$	90.35	24.29
5% Co-Fe$_2$O$_3$	82.41	26.25
10% Co-Fe$_2$O$_3$	175.16	53.19
5% Co-Fe$_2$O$_3$@NiO	117.74	29.20

by IMAGE-J software (Table 2) and presented as a histogram shown in inset (Figs. 2 and 3). The size of Co-doped α-Fe$_2$O$_3$ nanoparticles grows as the concentration of Cobalt increases; nanoparticle sizes are dependent on the concentration of cobalt (dopant) employed in sample synthesis, which is compatible with XRD data. To prove the existence of Co dopant and Ni, EDX characterization as shown in (Figs. 2e and 3c). It was performed on the Co-doped hematite nanoparticles. It clearly revealed the presence of iron, oxygen and cobalt as well and confirmed the formation of Co-doped Fe$_2$O$_3$ nanostructures. The observed percentage compositions of given elements as obtained by EDX agrees well with the calculated values shown in Table 3. The EDX spectrum (Fig. 3c) of 5% Co-Fe$_2$O$_3$@NiO shows the presence of Co and Ni, as suggested by the XRD results. In another word, the average particle size was increased from 82.41 to 117.74 nm during the coating of 5% Co-Fe$_2$O$_3$ with NiO.

Table 3 EDX analysis (atomic percent) of Co doped α-Fe_2O_3 and 5% Co-Fe_2O_3@NiO nanoparticles

	1% Co-Fe_2O_3	5% Co-Fe_2O_3	10% Co-Fe_2O_3	5% Co-Fe_2O_3@NiO
Fe (%)	40.57	43.23	35.28	40.32
O (%)	58.34	53.76	58.90	56.67
Fe/O	0.69	0.80	0.59	0.71
Co (%)	0.68	2.54	5.82	2.30
Ni (%)	–	–	–	0.72
Total	100	100	100	100

3.3 Fourier Transform Infra-Red (FT-IR) spectroscopy

Vibrational atoms of the pure and Co-doped α-Fe_2O_3, were analyzed by FT-IR technique (Fig. 4). The infrared spectrum of the synthesized pure and Co-doped α-Fe_2O_3 nanoparticles was between 400 and 4000 cm^{-1}. For the pure hematite uncalcined present broad absorption band centered at 3393 cm^{-1} and the peak at 1608 cm^{-1} is assigned to the stretching and bending vibrations of the hydroxyl groups and/or water molecules, respectively. In addition, there is a peak at 1432 cm^{-1} that is assigned to the deformation of CH_3. In addition to that, all organic species were eliminated after calcination. The FTIR spectrum of as-prepared iron oxide nanoparticles is shown in Fig. 4, which confirms the high purity of the sample. The band at 3500 cm^{-1} is assigned to adsorbed water which also gives rise to the stretching mode of hydroxyl at 3217 cm^{-1} and the bending mode of hydroxyl at 1650 cm^{-1} [30]. Other bands are as follows: 515 $cm^{-1}$and 423 cm^{-1} for Fe–O stretching mode of hematite and 468 cm^{-1} for lattice mode of FeO_6 [31]. The same results were obtained for Co-doped α-Fe_2O_3 (1, 5, and 10%).

3.4 Optical analysis

UV–vis diffuse reflectance spectra were used to investigate the optical properties of the as-prepared composites and the results are shown in Fig. 5a. The reflectance spectra of the hematite photoanodes were measured in the range of 200–800 nm. The gap energy for α-Fe_2O_3 (2.11 eV) corresponds well to the band gap values in the literature from 2.0 to 2.2 eV [21]. Optical absorption in the visible range has shown that α-Fe_2O_3 has immense potential as a photoanode material. Thus, an ideal photoanode requires a band gap which should be at least 1.6 eV, which corresponds to a start of absorption at 650 nm, to divide the water and faster electron transport.

The modified Kubelka–Munk function (Eq. 4) was used to produce the corresponding band gaps, as illustrated in Fig. 5b.

$$F(R_\infty) \equiv \frac{(1 - R_\infty)^2}{2R_\infty} = \frac{K}{S}, \tag{2}$$

$F(R_1)$ is the so-called remission or Kubelka–Munk function, where $R_1 = R_{sample} = R_{standard}$.

The band gap E_g and absorption coefficient of a direct band gap semiconductor is connected in the parabolic band structure by the well-known equation:

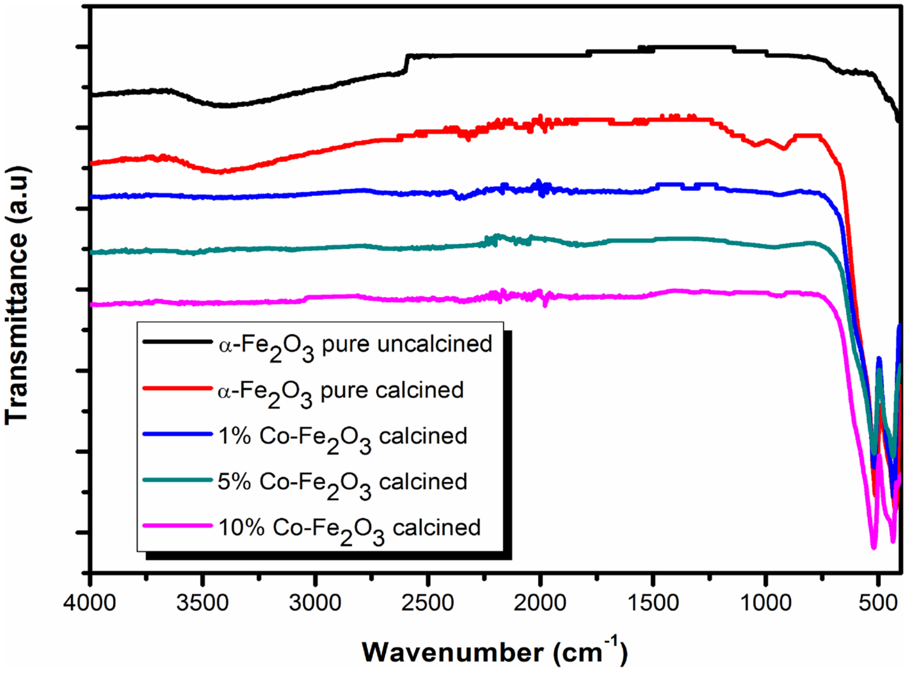

Fig. 4 FT-IR Spectra of pure α-Fe_2O_3 uncalcined, calcined at 800 °C and Co doped Fe_2O_3

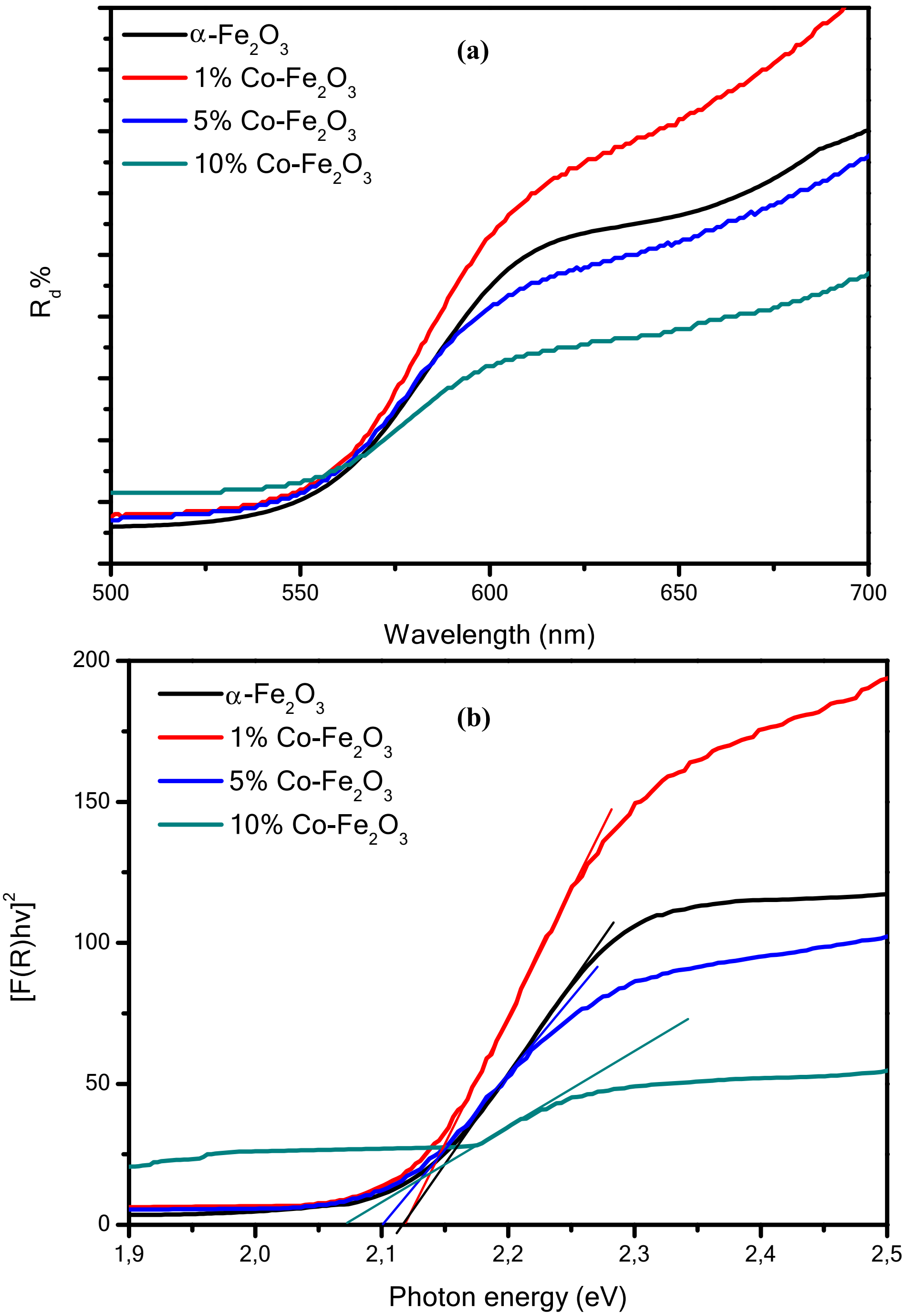

Fig. 5 **a** UV visible diffuse reflection spectra, **b** Band gap diagram calculated by Tauc plot of pure and Co-doped α-Fe$_2$O$_3$

$$\alpha h\nu = C_1\left(h\nu - E_g\right)^2, \tag{3}$$

where α is the linear absorption coefficient of the material, $h\,\nu$ is the photon energy and C_1 is proportionality constant. The K-M absorption coefficient K gets equal to 2 ($K=2$) when the material scatters perfectly diffusely. In this case, considering the K-M scattering coefficient S as constant with respect to wavelength, and using the remission function in Eq. (3) we obtain the expression:

$$\left[\frac{(1-R_\infty)^2}{2R_\infty}h\nu\right]^2 = C_2\left(h\nu - E_g\right). \tag{4}$$

Therefore, obtaining $F\,(R)$ from Eq. (2) and plotting the $[F\,(R)\,h\nu]^2$ against $h\nu$, the band gap E_g of a powder sample can be extracted easily.

The values obtained for the band gap energies of the pure, 1% Co-Fe$_2$O$_3$, 5% Co-Fe$_2$O$_3$ and 10% Co-Fe$_2$O$_3$ nanoparticles are 2.118–2.115–2.10 and 2.07 eV, respectively. Seeing that the gap energy of Co-Fe_2O_3 decreases compared to pure hematite that is in agreement with the results reported on Co-doped hematite nanoparticles prepared by other techniques [30]. This can be attributed to the magnetic properties and improvement of the electrical surface conductivity of Co-Fe_2O_3 [32].

3.5 Electrochemical measurement

The entire electrochemical studies were carried out using SCE as a reference electrode, platinum file as a counter electrode, and the active material coated GCE as a working electrode in 1 M NaOH alkaline solution has been displayed in Fig. 6. Hematite was considered one of the most promising candidates for potential application with the withstanding to the pseudocapacitance and normal electric double-layer capacitance by the following redox reaction [33]:

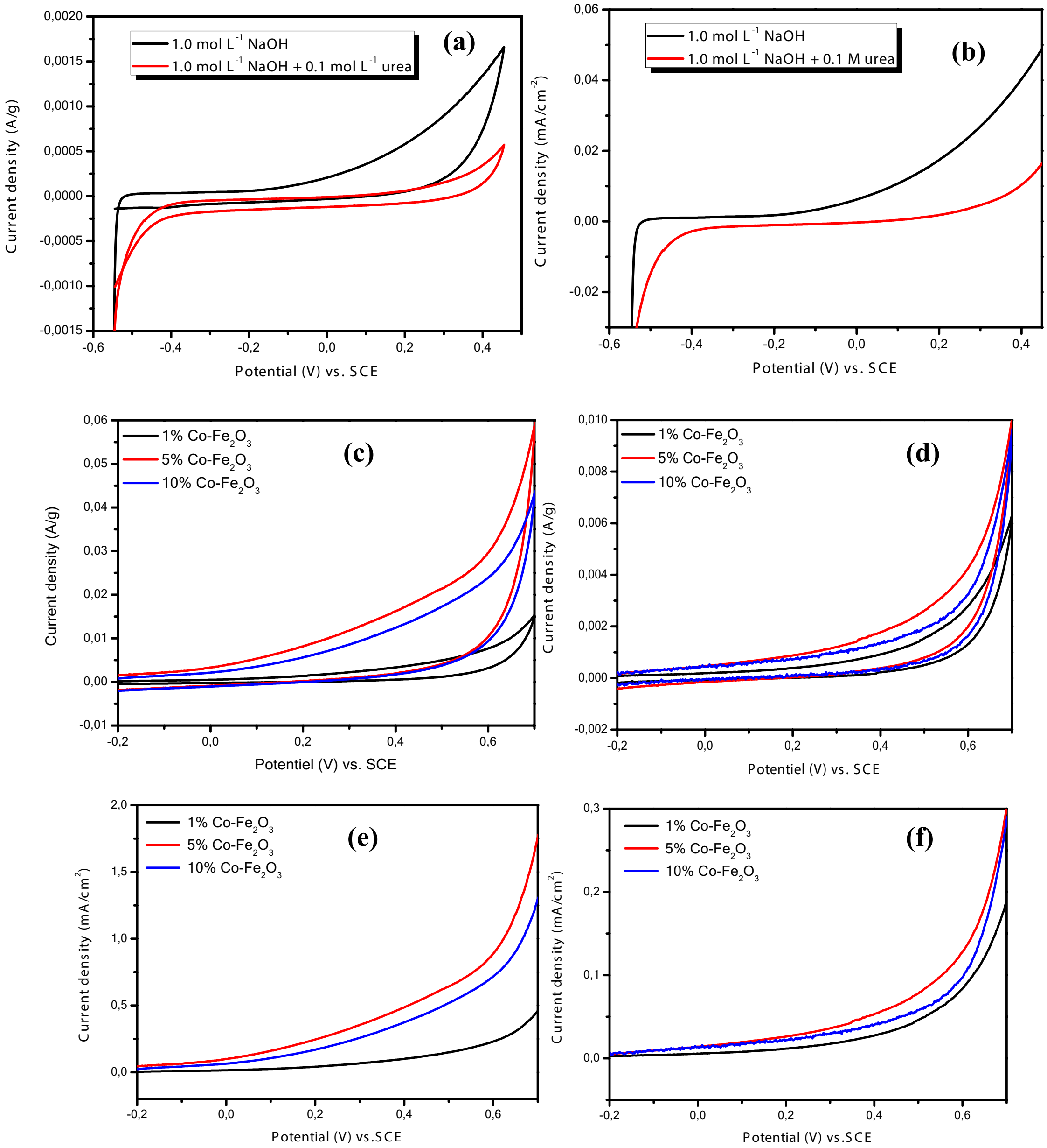

Fig. 6 **a** CV graph and **b** LSV graph obtained in 1.0 M NaOH in the absence and presence of 0.1 M urea of pure α-Fe_2O_3 electrode; CV responses obtained in 1.0 M NaOH in **c** the absence, **d** presence of 0.1 M urea and **e** linear sweep voltammetry plots in 1.0 M NaOH in the absence and **f** presence of 0.1 M urea of Co-Fe_2O_3 electrode with a scan rate of 10 mV/s

$$Fe_2O_3 + OH^- \leftrightarrow Fe_2O_3OH + e^-. \tag{5}$$

The specific capacitance is the phenomenon which completely supports the OER analysis of the respective samples. Hence, the specific capacitance has been calculated from the formula,

$$C = \frac{\int_{V1}^{V2} I(V)dV}{\left(V_2 - V_1\right)Sm}, \tag{6}$$

where (I (V) dV) the area of the CV curve, the mass of the active material (m) layered on the graphite substrate, the scan rate value (S) and the potential window difference ($V_2 - V_1$) have been substituted in the above formula. The obtained values have been tabulated in Table 4.

As per the formula, the highest specific capacitance is observed for the sample 5% Co-Fe_2O_3 and the highest OER activity is also expected for the same sample. The overall improvement in the specific capacity and electrochemical performance of Co doped hematite compared to the naked sample may be due to the percentage of the dopant. Divalent Co^{2+} as an electron donor in the hematite nanostructure, which increases the conductivity and density transport of the charge carrier across the space charge layer. Consequently, the increase in the electronic conductivity of hematite by the dopant Co. The CV curve observed for 5% of Co- Fe_2O_3 is mainly governed by the faradic redox reaction:

$$Co^{2+} \leftrightarrow Co^{3+} + e^-. \tag{7}$$

The specific capacities are low compared to those reported in the literature for α-Fe_2O_3 and 1% Co-Fe_2O_3 in alkaline medium and in urea. According to Abdi et al. [34], can be attributed to the processing temperature of α-Fe_2O_3 (800 °C). Then, an inverse relationship between the processing temperature and the specific capacity was confirmed [34]. In addition, the decrease in ionic conductivity, due to the decrease in the hydrated state, as well as the decrease in both the accessibility of the electrolyte to the pores and the reactivity of the oxide [35].

Figure 6e shows the linear scanning voltammetry (LSV) graph of bare Co-doped α-Fe_2O_3 nanostructures at scan rate of 10 mV/s. It also shows that the sample, which possessed the highest specific capacitance, has a good oxygen evolution reaction (OER) activity. The electrochemical OER activity of the best performed samples is reported 0.04 (0.4 V vs. SCE), 0.149, 0.650 and 0.523 mA/cm^2 (at 0.5 V vs. SCE) for α-Fe_2O_3, 1% Co-Fe_2O_3, 5% Co-Fe_2O_3 and 10% Co-Fe_2O_3, respectively, confirmed by LSV spectra. Hence, the highest OER activity observed for 5% Co-Fe_2O_3 samples may be due to the inbuilt catalytic activity of Co explained by the increasing electron transfer as well as to the combined effect of nanoparticle morphology or the formation of new active centers on the hematite nanostructure due to Co doping and oxygen vacancies and favorable band gap.

3.6 Electrocatalytic oxidation of urea

The electrocatalytic activity of 5% Co-Fe_2O_3@NiO without annealing electrocatalyst was studied by scanning in a 1 M NaOH solution containing 0.10 M urea at 10 mVs^{-1} in Fig. 7a an oxidation peak was started at a potential value of 370 mV. Its maximum oxidation current density was recorded at a potential value of 450 mV. While observing the CV trace of 5% Co-Fe_2O_3@NiO electrode with annealing, the oxidation peak potential of 5% Co-Fe_2O_3@NiO electrode was observed at + 0.457 V. In the reverse scan, a peak has also been observed, which could be linked to the oxidation of the adsorbed species during the electro-oxidation of urea [36]. Increased values of oxidation current density were observed between with and without calcination, which can be explained by the increase in the content of nickel oxide in the electrocatalyst produced

Table 4 Specific capacitance values calculated from CV graph undoped and Co doped Fe_2O_3 nanostructures

Sample	Specific capacitance calculated from CV (F/g) at 10 mV/s	Current density LSV at 10 mV/s at 0.5 V vs SCE (mA/cm^2)	Current density LSV at 10 mV/s at 0.5 V vs SCE (mA/g)
NaOH			
α-Fe_2O_3	26.98	0.04 (0.4 V vs. SCE)	1.34 (0.4 V vs. SCE)
1% Co-Fe_2O_3	81.63	0.149	5.02
5% Co-Fe_2O_3	352.11	0.650	21.673
10% Co-Fe_2O_3	281.70	0.523	17.376
NaOH + Urea			
α-Fe_2O_3	15.61	0.01 (0.4 V vs. SCE)	0.35 (0.4 V vs. SCE)
1% Co-Fe_2O_3	24.57	0.048	1.518
5% Co-Fe_2O_3	44.60	0.175	2.631
10% Co-Fe_2O_3	33.97	0.058	1.978

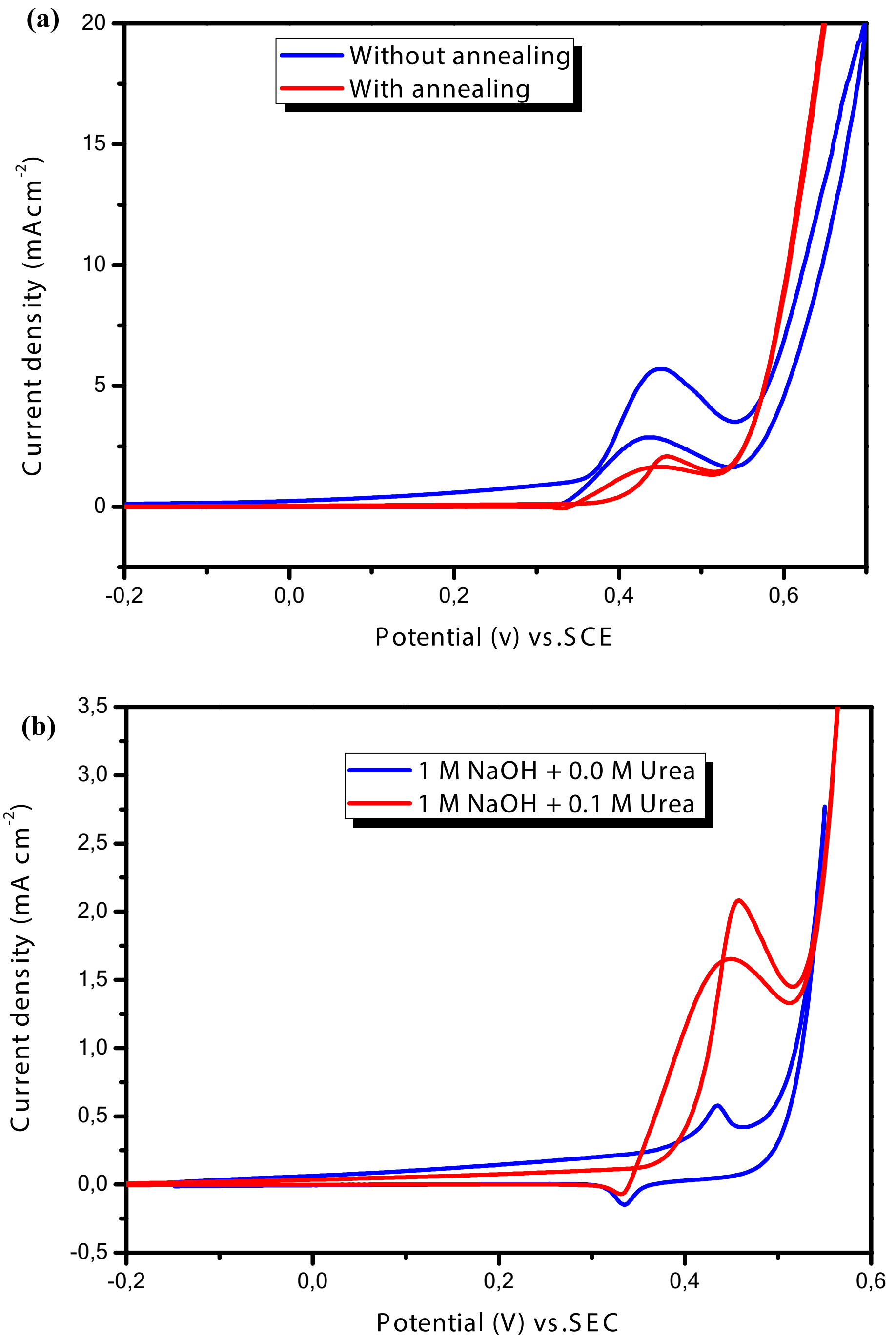

Fig. 7 CV responses for 5% Co-Fe_2O_3@NiO/GC in 1 M NaOH; **a** with/without annealing, **b** in absence/presence of 0.1 M urea using scan rate of 10 mV s^{-1}

and as a moderate to good electrochemical catalyst for OER [37]. The 5% Co-Fe_2O_3@NiO electrode without calcination had an oxidation peak current density of 5.728 mA cm^{-2} in the presence of 0.1 M urea in 1.0 M NaOH 3.6 times more than that of 5% Co-Fe_2O_3@NiO electrode with calcination (1.59 mA/cm^2). The feasibility of the direct use of 5% Co-Fe_2O_3@NiO as an anode material for urea electrooxidation was tested by CV measurements at a scan rate of 10 mV s^{-1}, as shown in Fig. 7b. Figure 7b shows the responses of 5% Co-Fe_2O_3/NiO in the absence and in the presence of 0.1 M urea in 1 M NaOH. During the absence of urea, two redox peaks can be observed at 435 mV and 334 mV in the anode and cathode branches, respectively, can be explained by the reversible transformation between $Ni(OH)_2$ and the species at redox couple NiOOH [38]. Where the anode peak is linked to the oxidation of Ni (II) to Ni (III), while the cathode peak corresponds to the reduction of Ni (III) to Ni (II) [39]. According to the literature, the Ni^{2+}/Ni^{3+} transformation can occur by two routes: a solvent mechanism in which nickel oxyhydroxide (γ-NiOOH) is formed by OH^- diffusion according to Eq. 8, and by the proton scattering mechanism in which β-NiOOH is probably produced (Eq. 9) [40]

$$Ni\ (OH)_2 + OH^- \rightarrow H_2O + \gamma\text{ - }NiOOH + e^-, \tag{8}$$

$$Ni\ (OH)_2 \leftrightarrow H^+ + \beta\text{ - }NiOOH + e^-, \tag{9}$$

When urea is present, an anodic peak of high current at 0.457 V is noted, which indicates a reinforcement of the electro-oxidation of urea on the modified electrode 5% Co-Fe_2O_3@NiO/ GC. An additional anode peak is observed at −0.444 V in the reverse scan, which is located in the oxidation range of urea which due to the continued electrooxidation of urea due to the renewal of the active sites (Ni (II)/Ni (III)) on the surface of the electrode. Seeing that the anode peak in the reverse scan is smaller than that in the direct scan due to the imperfect renovation of the active centers on the modified electrode interface. The electrocatalytic mechanism of urea in NaOH media on the electrode modified with 5% Co-Fe_2O_3@ NiO can be described as:

$$6OH^- + CO\left(NH_2\right)_{2(aq)} \rightarrow 5H_2O + CO_{2(g)} + N_{2(g)} + 6e^-. \tag{10}$$

At cathode:

$$6H_2O + 6e^- \rightarrow 6OH-_{(aq)} + 3H_{2(g)}. \tag{11}$$

Overall reaction:

$$CO\left(NH_2\right)_{2(aq)} + H_2O \rightarrow 3H_{2(g)} + CO_{2(g)} + N_{2(g)}. \tag{12}$$

However, when there is no urea, the potential is only used for the electrooxidation of Ni (II) to Ni (III). The large difference in current density between the solution with and without urea is due to the electro-oxidation of urea. The behavior could be related to the large surface of 5% Co-Fe_2O_3@NiO, which can improve the current density, favor the transfer of electrons. The discussion of Fig. 7a impliques the reversibility of the NiOOH/$Ni(OH)_2$ peak in the 1 M NaOH solution and in presence of urea, the regeneration of the $Ni(OH)_2$ catalyst will lead to the loss of reversibility of the NiOOH/$Ni(OH)_2$ peak and hence the anodic current density increases drastically [23].

$$Ni(OH)_{2(s)} + OH^- \rightarrow NiOOH_{(s)} + H_2O_{(l)} + e^-, \tag{13}$$

$$NiOOH_{(s)} + urea_{(aq)} \rightarrow Ni(OH)_{2(s)} + products. \tag{14}$$

The above two equations imply the catalyst regeneration as per the indirect oxidation of urea. This is in accordance with the nice work done by Botte et al. [41].

3.7 Photoelectrochemical measurement

Photoelectrochemical measurements of the α-Fe_2O_3, Co-Fe_2O_3, and Co-Fe_2O_3@NiO films were carried out in an aqueous solution of 1.0 M NaOH with or without urea under 500 W/m^2 of illumination light to study the photoelectrochemical oxidation performance of urea, as shown in the figure. The films were made by spin coating and annealing at 800 °C. High-temperature annealing of the α-Fe_2O_3 films on the FTO substrate, according to Shaohua Shen, could increase their PEC performance for water splitting. Explained by Sn diffusion from the FTO substrate into Fe_2O_3, which is assured by high-temperature annealing and resulting in an electrical alteration of α -Fe_2O_3 films, which improved the photoactivity of doped hematite nanostructures. The current–voltage characteristics of the α-Fe_2O_3 measured in both the dark and illumination were shown in Fig. 8a, b it is clear that the current density is quite constant between 0.0 and 0.3 V, but then increases with the applied potential. In 1 M NaOH with 0.1 M urea, α-Fe_2O_3 has a photocurrent density of 1.8 μA/cm^2 at 0.5 V vs. SCE and 1.7 μA/cm^2 in 1 M NaOH with 0.1 M urea. The good light absorption, efficient electron transfer, and charge separation of the α-Fe_2O_3/FTO nanocomposite are responsible for the large increase in photocurrent for this electrode when compared to others [22, 42, 43] created by a similar approach.

Then, the I-t photocurrent density experiments under simulated sunlight were carried out with the light on/off shown in Fig. 8c, d, the quasi-stability and reproducibility of the photocurrent signal, that any overshoot was observed at the beginning or the end of the On/Off cycle, this is explained by the creation of traps that hinder electron movement in addition to the slowdown of the photocurrent generation [44] was caused by the direction of electron diffusion was apparently free of grain boundaries.

Figure 9a, b shows the variation in the photocurrent intensity of the Co-doped α-Fe_2O_3 electrodes. It is worth noting the decrease of the photocurrent from 1.7 μA/cm^2 vs. SCE to about 0.5 μA/cm^2 vs. SCE with the Co doping. However, adverse effects may take place at high modifier concentration [45]. Thus there exists an optimal modifier concentration [46]. At high concentrations, Co^{2+} would have defect scattering/ recombination properties and finally negate the increased separation efficiency.

The stability and reproducibility of the photocurrent signal are seen in the figure. No overshoot was observed at the start or end of the On/Off cycle shown in Fig. 9c, d, indicating that the direction of electron scattering was apparently free of grain boundaries, which can create traps that hinder the movement of electrons and slow down the generation of photocurrents [44].

In alkaline medium, Co-Fe_2O_3@NiO gives a pair of redox peaks corresponding to the $Ni(OH)_2$ / NiOOH conversion

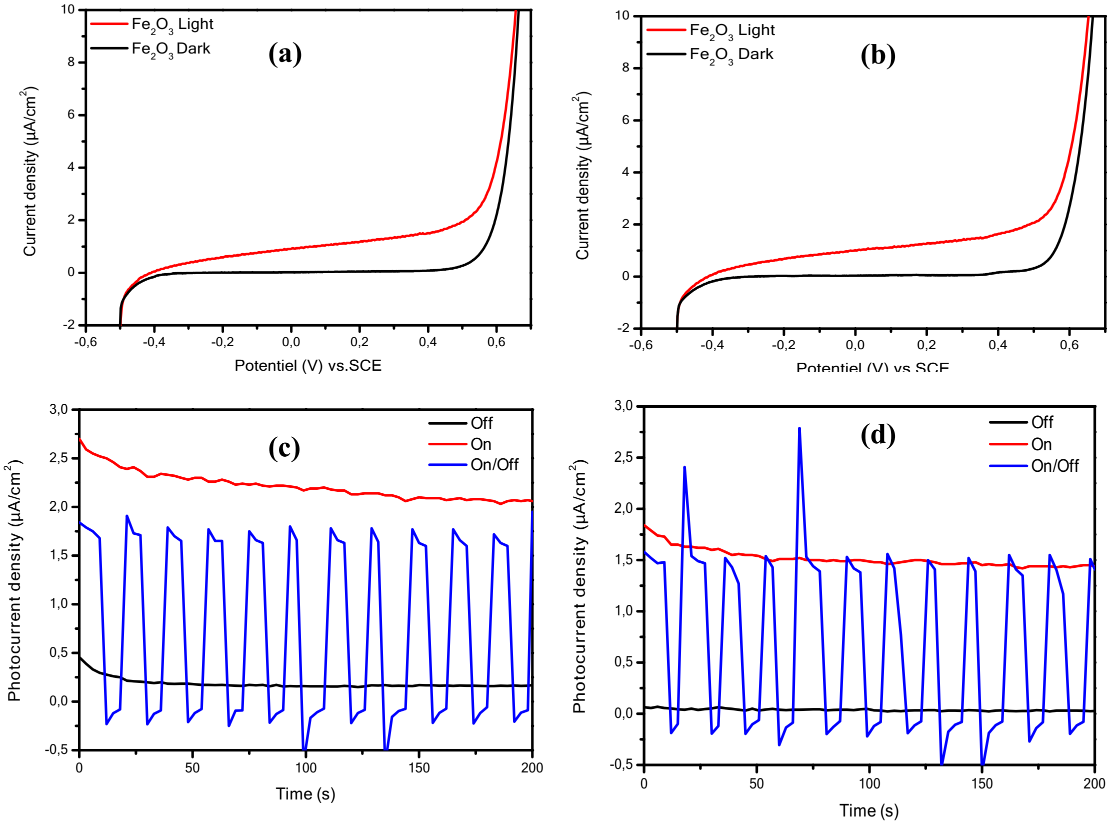

Fig. 8 Linear Sweep Voltammetry plots in the dark and with illumination at a scan rate of 10 mVs^{-1}; **a** in 1 M NaOH, **b** 1 M NaOH with 0.1 M urea and photocurrent responses recorded at 0.4 V vs. SCE for the undoped α-Fe_2O_3 electrodes in successive illumination cycles **c** in 1 M NaOH, **d** 1 M NaOH with 0.1 M urea

reaction (Fig. 10). The current density in the dark was measured at 8.67 µA/cm^2. In contrast, 11.73 µA/cm^2 was the result under the irradiation of simulated sunlight. The photoanode 5% Co-Fe_2O_3@NiO has photocurrent states equal to 3.07 µA/cm^2.

In the presence of urea, The oxidative current has resulted from the oxidative reaction of $Ni(OH)_2$ to NiOOH at 0.3 V, urea facilitated the oxidative reaction of $Ni(OH)_2$ to NiOOH at 0.3 V that implicated an oxidative current by the Electrochemical (E-C) process (Eqs. (15) and (16)). In addition to that, the increasing oxidative current is ascribed to the oxidative reaction of $Ni(OH)_2$ to NiOOH was presented in the reverse scan. It is clear that the reduction peak of NiOOH to $Ni(OH)_2$ in the presence of urea is weaker than that without urea, however, the reduction peak of NiOOH to $Ni(OH)_2$ in the presence of urea is weaker than that without urea, this due to the consumption of a part of the active sites of NiOOH by urea through indirect oxidation process (Eq. 15) [47].

$$Ni(OH)_2 + OH^- \leftrightarrow +NiOOH + H_2O + e^-, \tag{15}$$

$$6NiOOH + CO(NH_2)_2 + H_2O \rightarrow H_2O + N_2 + CO_2. \tag{16}$$

Thus we see an improvement in the density of the photocurrent from 3.06 to 42.21 µA/cm^2 during the photocatalytic oxidation of urea (Table 5).

The I-t curve of the 5% Co-Fe_2O_3/NiO photoanode also has a relatively regular undulation with the light activation/deactivation cycles (Fig. 11) with a current density decay was noticed at the early stage of chronoamperograms in 1 M NaOH with 0.1 M urea. As can be seen in Fig. 11, it should be noted that the 5% Co-Fe_2O_3@NiO film has excellent photocurrent improvements and the photocurrent is superior to the Fe_2O_3 film or 5% Co-Fe_2O_3. A weak overshoot was observed at the end of the On/Off cycle, which indicates that the rectangular response illustrates that the direction of electron diffusion was apparently free of grain boundaries, which can create traps that hinder electron movement and slow down photocurrent generation [48].

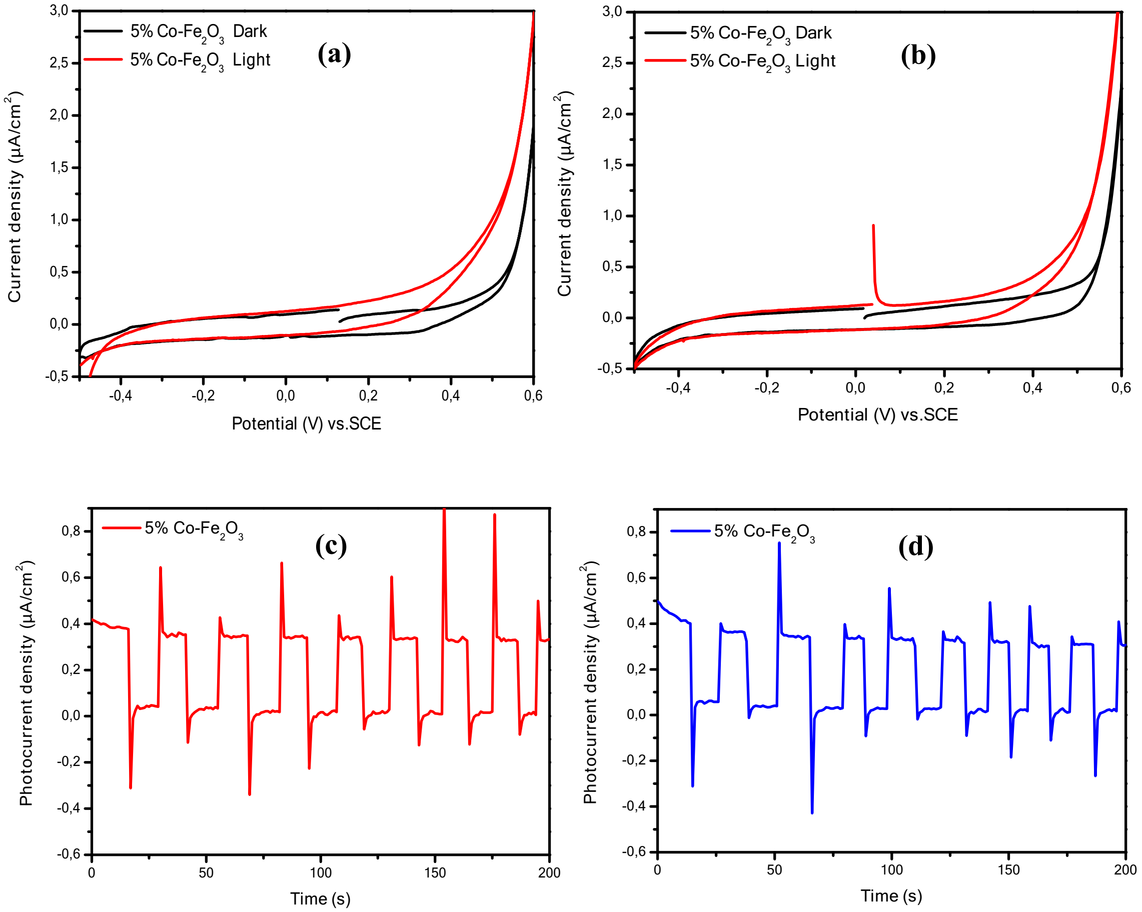

Fig. 9 CV plots in the dark and with illumination at a scan rate of 10 mVs^{-1}; **a** in 1 M NaOH, **b** 1 M NaOH with 0.1 M urea and photocurrent responses recorded at 0.4 V vs. SCE for the 5% Co-Fe_2O_3 electrodes in successive illumination cycles **c** in 1 M NaOH, **d** 1 M NaOH with 0.1 M urea

4 Conclusion

In summary, a microwave-assisted synthesis route has been used for the fabrication of composite materials with a high crystalline nature and purity, which is much faster, cleaner and more energy-efficient than conventional methods. It was implemented to construct Co-Fe_2O_3@NiO core–shell nanocomposites from the Co-Fe_2O_3 nanoparticles synthesized by the co-precipitation method. The hexagonal crystal structure of the synthesized nanoparticles was revealed by XRD analysis, confirming no structural change upon doping with Co. An increase in average grain size was observed by Co doping calculated by IMAGE-J software SEM. The presence of Co and Ni in Co-Fe_2O_3 and Co-Fe_2O_3@NiO was confirmed by EDX analysis. Other analysis were performed such us FTIR and UV–vis. The nanocomposite has been designed and utilized as an effective electrocatalyst for urea oxidation in alkaline medium (1.0 M NaOH), although various methods including CV, and Chronoamperometric measurements were utilized for investigation of the electrochemical features of urea electrooxidation. The Co dopant helped as an ionized donor and helps in increasing the carrier density of the α-Fe_2O_3 films. The main effect of Co atoms on Fe_2O_3 is the enhancement of the charge transport properties and conductivity. The 5% Co-Fe_2O_3 exhibits a high specific capacity of 352.11 Fg^{-1} at a current density of 0.650 mA/cm^2. In other cases, the Co-Fe_2O_3@NiO photoanode showed 23 times increase in photocurrent density under illumination than α-Fe_2O_3 and 80 times than Co-Fe_2O_3 while the photoelectrochemical oxidation of urea. These findings demonstrate the superior performance of the prepared Co-Fe_2O_3@NiO thin films provided potential applications in photocatalysis for water splitting and in the conversion photoelectrochemical of urea and application in fuel cells and for hydrogen production.

Fig. 10 The I-V characteristics of the Co-Fe_2O_3@NiO electrode; **a** in alkaline medium, **b** in presence of 0.1 M urea in the dark and with illumination at a scan rate of 10 mV/s

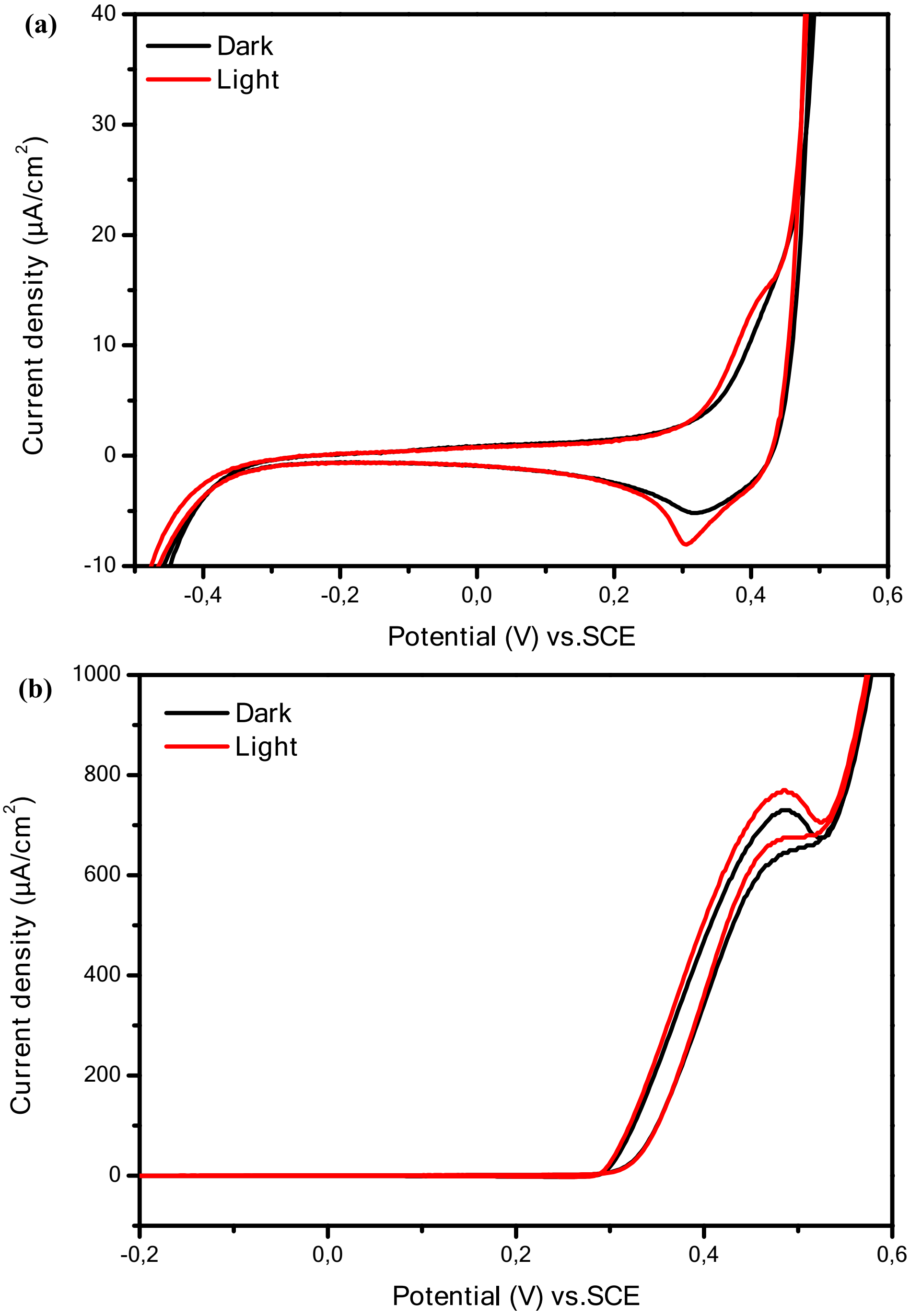

Table 5 Photocurrent density in alkaline medium and in presence of urea in the dark and with illumination of pure, Co doped hematite and Co-Fe_2O_3@NiO at a scan rate of 10 mVs^{-1}

Sample	1 M NaOH			1M NaOH + 0.1 M Urea		
	Under illumination (μAcm^{-2})	In the Dark (μAcm^{-2})	Photocurrent intensity (μAcm^{-2})	Under illumination (μAcm^{-2})	In the Dark (μAcm^{-2})	Photocurrent intensity (μAcm^{-2})
α-Fe_2O_3	2	0.291	1.709	2.133	0.337	1.8
5% Co-Fe_2O_3	0.869	0.346	0.523	0.866	0.342	0.524
5% Co-Fe_2O_3@NiO	11.73	8.67	3.06	756.49	714.28	42.21

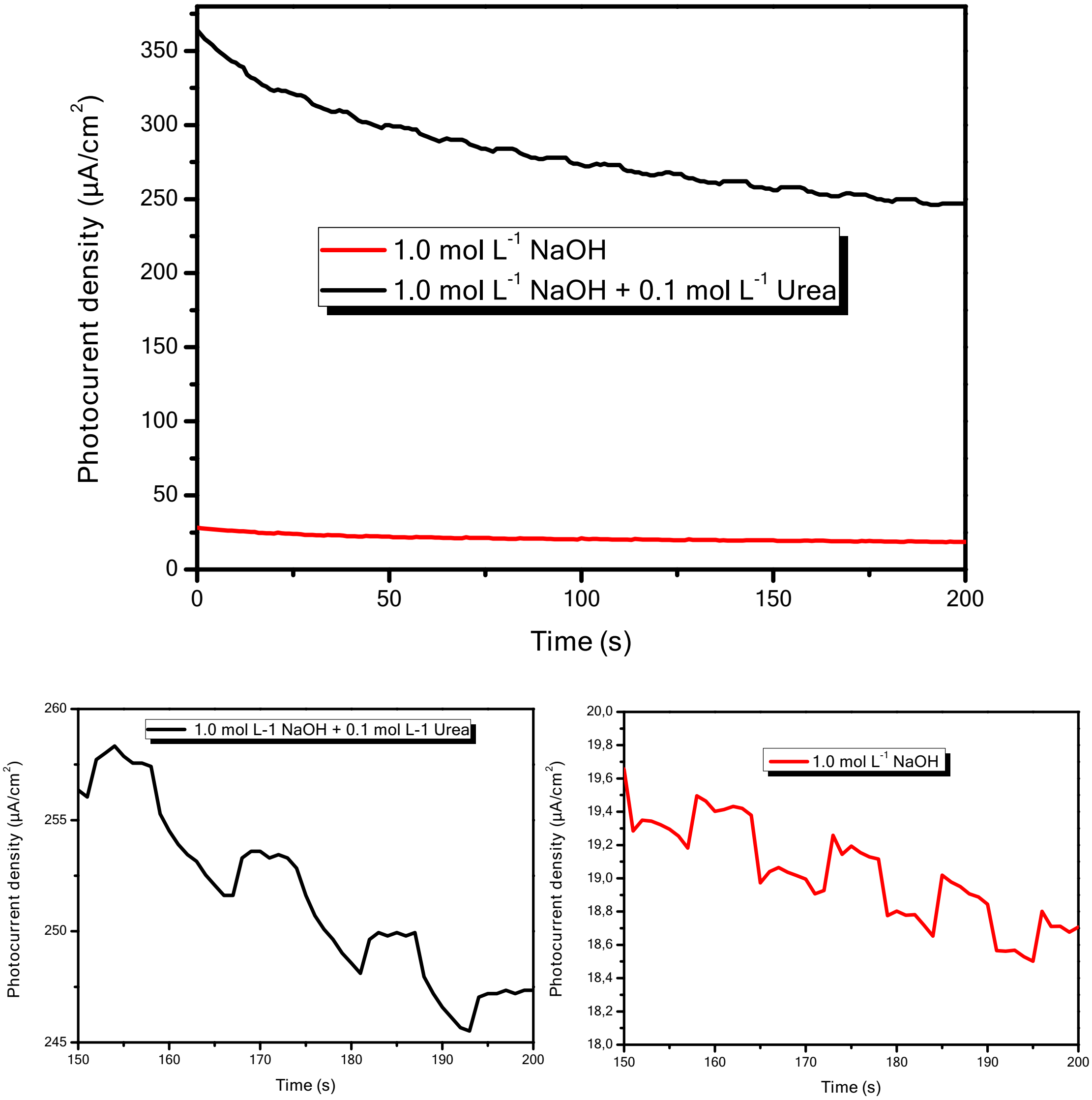

Fig. 11 The chronoamperometric measurements for the Co-Fe_2O_3@NiO electrode under On/Off illumination conditions measured in the absence and presence of urea with a bias potential of 0.4 V vs. SCE

Acknowledgements The present work was supported by the Research Funds of Electrochemistry, Materials and Environment Research Unit UREME (UR17ES45), Faculty of Sciences Gabes University, Tunisia and Institute of Chemistry and Materials Paris-Est (ICMPE, UMR7182) Thiais, University of Creteil, France.

Funding This work was funded by the Ministry of Higher Education and Scientific Research of Tunisia and received no external funding.

Declarations

Conflict of interest The authors declare that they have no conflict of interest.

References

1. Van de Krol R, Liang Y, Schoonman J (2008) J Mater Chem 18(20):2311–2320
2. Vesborg PC, Jaramillo TF (2012) RSC Adv 2(21):7933–7947
3. Kazim A, Veziroglu TN (2001) Renew Energy 24(2):259–274
4. Jiao Y, Zheng Y, Jaroniec M, Qiao SZ (2015) Chem Soc Rev 44(8):2060–2086
5. Larcher D, Tarascon JM (2015) Nat Chem 7(1):19–29
6. Qiu Y, Leung SF, Zhang Q, Hua B, Lin Q, Wei Z, Fan Z (2014) Nano Lett 14(4):2123–2129
7. Lu Y, Cheng X, Tian G, Zhao H, He L, Hu J, Su BL (2018) Nano Energy 47:8–17
8. Wang H, Kong H, Pu Z, Li Y, Hu X (2020) Energy Convers Manag 210:112699
9. Khan SU, Akikusa J (1999) J Phys Chem B 103(34):7184–7189
10. Soares L, Alves A (2018) Mater Lett 211:339–342

11. Zhan F, Li J, Li W, Liu Y, Xie R, Yang Y, Chen Q (2015) Int J Hydrogen Energy 40(20):6512–6520
12. Liu W, Yang Y, Zhan F, Li D, Li Y, Tang X, Li J (2018) Int J Hydrogen Energy 43(18):8770–8778
13. Kim TW, Choi KS (2014) Science 343(6174):990–994
14. Li T, He J, Peña B, Berlinguette CP (2016) Angew Chem Int Ed 55(5):1769–1772
15. Wang W, Dong J, Ye X, Li Y, Ma Y, Qi L (2016) Small 12(11):1469–1478
16. Chaudhary D, Singh S, Vankar VD, Khare N (2017) Int J Hydrogen Energy 42(12):7826–7835
17. Jaramillo TF, Baeck SH, Kleiman-Shwarsctein A, Choi KS, Stucky GD, Mc Farland EW (2005) J Comb Chem 7(2):264–271
18. Ye YQ, Gu GH, Wang XT, Ouyang T, Chen Y, Liu ZQ (2019) Int J Hydrogen Energy 44(39):21865–21872
19. Wu L, Tsui LK, Swami N, Zangari G (2010) J Phys Chem C 114(26):11551–11556
20. Konta R, Ishii T, Kato H, Kudo A (2004) J Phys Chem B 108(26):8992–8995
21. Wang D, Chen Y, Zhang Y, Zhang X, Suzuki N, Terashima C (2017) Appl Surf Sci 422:913–920
22. Janu VC, Bahuguna G, Laishram D, Shejale KP, Kumar N, Sharma RK, Gupta R (2018) Sol Energy Mater Sol Cells 174:240–247
23. Bian L, Du Q, Luo M, Qu L, Li M (2017) Int J Hydrogen Energy 42(40):25244–25250
24. Ahmadi A, Nezamzadeh-Ejhieh A (2017) J Electroanal Chem 801:328–337
25. Glass DE, Galvan V, Prakash GS (2017) Electrochim Acta 253:489–497
26. Supattarasakda K, Petcharoen K, Permpool T, Sirivat A, Lerdwijitjarud W (2013) Powder Technol 249:353–359
27. Hua J, Gengsheng J (2009) Mater Lett 63(30):2725–2727
28. Huerta-Flores AM, Chávez-Angulo G, Carrasco-Jaim OA, Torres-Martínez LM, Garza-Navarro MA (2021) J Photochem Photobiol 410:113077
29. Satheesh R, Vignesh K, Suganthi A, Rajarajan M (2014) J Environ Chem Eng 2(4):1956–1968
30. Suresh R, Prabu R, Vijayaraj A, Giribabu K, Stephen A, Narayanan V (2012) Mater Chem Phys 134(2–3):590–596
31. Al-Kady AS, Gaber M, Hussein MM, Ebeid EZM (2011) Spectrochim Acta Part A Mol Biomol Spectrosc 83(1):398–405
32. Morales AE, Mora ES, Pal U (2007) Revista mexicana de física 53(5):18–22
33. Rani BJ, Kumar MP, Ravi G, Ravichandran S, Guduru RK, Yuvakkumar R (2019) Appl Surf Sci 471:733–744
34. Abdi A, Trari M (2013) Electrochim Acta 111:869–875
35. Lee MT, Chang JK, Hsieh YT, Tsai WT (2008) J Power Sources 185(2):1550–1556
36. Guo F, Ye K, Cheng K, Wang G, Cao D (2015) J Power Sources 278:562–568
37. Kou X, Xin X, Zhang Y, Meng LY (2021) Carbon Lett 31(4):695–706
38. Tammam RH, Saleh MM (2017) J Electroanal Chem 794:189–196
39. Fathi AM, Handal HT, El-Kady AA (2021) Carbon Lett 31(2):253–267
40. Abd El-Lateef HM, Almulhim NF, Alaulamie AA, Saleh MM, Mohamed IM (2020) Colloid Surf A 585:124092
41. Vedharathinam V, Botte GG (2013) Electrochim Acta 108:660–665
42. Yin S, Wang X, Mou Z, Wu Y, Huang H, Zhu M, Yang P (2014) Phys Chem Chem Phys 16(23):11289–11296
43. Chu D, Li K, Liu A, Huang J, Zhang C, Yang P, Lu C (2018) Int J Hydrogen Energy 43(15):7307–7316
44. Sookhakian M, Amin YM, Baradaran S, Tajabadi MT, Golsheikh AM, Basirun WJ (2014) Thin Solid Films 552:204–211
45. Iervolino G, Tantis I, Sygellou L, Vaiano V, Sannino D, Lianos P (2017) Appl Surf Sci 400:176–183
46. Atabaev TS, Ajmal M, Hong NH, Kim HK, Hwang YH (2015) Appl Phys A 118(4):1539–1542
47. Guo F, Ye K, Du M, Huang X, Cheng K, Wang G, Cao D (2016) Electrochim Acta 210:474–482
48. Yoshida T, Zhang J, Komatsu D, Sawatani S, Minoura H, Pauporté T, Yanagi H (2009) Adv Func Mater 19(1):17–43